

# A Theory of Single-Antenna Atomic Beamforming

Mingyao Cui, Qunsong Zeng, and Kaibin Huang, *Fellow, IEEE*

**Abstract**—Leveraging the quantum advantages of highly excited atoms, Rydberg atomic receivers (RAREs) represent a paradigm shift in radio wave detection, offering high sensitivity and broadband reception. However, existing studies largely model RAREs as isotropic point receivers and overlook the spatial variations of atomic quantum states within vapor cells, thus inaccurately characterizing their reception patterns. To address this issue, we present a theoretical analysis of the aforementioned spatial responses of a standard local-oscillator (LO)-dressed RARE. Our results reveal that increasing the vapor-cell length produces a receive beam aligned with the LO field, with a beamwidth inversely proportional to the cell length. This finding enables atomic beamforming to enhance received signal-to-noise ratio using only a single-antenna RARE. Furthermore, we derive the achievable beamforming gain by characterizing and balancing the fundamental tradeoff between the effects of increasing the vapor cell length and the exponential power decay of laser propagating through the cell. To overcome the limitation imposed by exponential decay, we propose a novel RARE architecture termed segmental vapor cell. This architecture consists of vapor-cell segments separated by clear-air gaps, allowing the total cell length (and hence propagation loss) to remain fixed while the effective cell length increases. As a result, this segmented design expands the effective atom-field interaction area without increasing the total vapor cell length, yielding a narrower beamwidth and thus higher beamforming gain as compared with a traditional continuous vapor cell.

**Index Terms**—Quantum sensing, Rydberg atomic receivers, atomic beamforming, wireless communications.

## I. INTRODUCTION

The rapid advancement in quantum information science and technology is poised to revolutionize the fields of computation, communication, and sensing [1]. Among these, quantum sensing stands out as particularly promising due to its potential to enable a wide range of applications and thereby significantly impact society [2], [3]. By harnessing quantum phenomena such as entanglement and quantum state squeezing, these technologies offer measurement sensitivities that surpass classical limits. The paradigm shift has led to the development of various high-precision quantum sensors, including magnetometers, gravimeters, and electrometers, which have propelled advances in physics, metrology, geophysics, and communications [2]. Building upon these quantum advancements, Rydberg atomic receivers (RAREs) are expected to influence wireless communication by enabling high-precision detection of radio-frequency (RF) electric fields [4]. The focus of this work is the development of novel RARE-enabled wireless communication techniques.

RAREs operate on quantum-mechanical principles that are fundamentally different from those of classical RF re-

M. Cui, Q. Zeng, and K. Huang are with Department of Electrical and Electronic Engineering, The University of Hong Kong, Hong Kong (Emails: {mycui, qszeng}@eee.hku.hk, huangkb@hku.hk). Corresponding authors: Q. Zeng; K. Huang.

ceivers [5]. Specifically, rather than using metallic antennas to transduce RF signals into electrical currents, RAREs employ *quantum antennas*, referring to alkali-metal atoms with highly excited Rydberg states. When exposed to external RF fields, these atoms undergo transitions between Rydberg energy levels, inducing measurable shifts in their optical transmission spectra. To detect these shifts, laser beams are propagated through a vapor cell containing these Rydberg atoms, and the output light is monitored using photodetectors (PDs) [6]. This all-optical transduction enables direct RF-to-baseband conversion without the need for traditional electronic front-end components. As a result, RAREs bypass the thermal noise limits imposed by Johnson-Nyquist noise [7]. Theoretically, RAREs can approach the standard quantum limit (SQL) of sensitivity, approximately  $\sim 700 \text{ pV} \cdot \text{cm}^{-1} \cdot \text{Hz}^{-1/2}$  [8], which is lower than the thermal noise floor of about  $\sim 0.98 \text{ nV} \cdot \text{cm}^{-1} \cdot \text{Hz}^{-1/2}$  [9]. In addition to their high sensitivity, RAREs offer several other advantages. On one hand, a single RARE device can provide ultra-broadband coverage—from DC up to the terahertz regime—by leveraging the so-called AC Stark shift and the dense atomic energy levels [10], [11]. In contrast, classical receivers require multiple band-specific hardware components to detect signals across different bands. On the other hand, when configured as an array, RAREs exhibit negligible mutual coupling, which is an issue that commonly affects traditional arrays. This is attributed to the minimal interaction between spatially separated laser beams [4]. With these distinctive features, the deployment of RAREs in next-generation wireless systems promises to achieve unprecedented sensitivity, connectivity, and spectral efficiency.

Though research on RAREs remains in its early stages, recent efforts have significantly advanced the field along three primary directions. First, there has been continuous progress in the development of RARE architectures, aimed at demonstrating signal detection capability, enhancing sensitivity, and improving system compactness. The foundational RARE architecture relies on two quantum phenomena, electromagnetically induced transparency (EIT) and Autler-Townes (AT) splitting [6], [12], achieving sensitivities on the order of  $\sim \mu\text{V} \cdot \text{cm}^{-1} \cdot \text{Hz}^{-1/2}$ . The need for frequency scanning of a laser beam for observing EIT-AT can be eliminated by incorporating an external local oscillator (LO) field, leading to the *superheterodyne* architecture [8]. Such LO-dressed RARE systems have achieved remarkable sensitivity of approximately  $1 \text{nV} \cdot \text{cm}^{-1} \cdot \text{Hz}^{-1/2}$  [8], [13]. Most recently, the *self-heterodyne* detection architecture has been proposed for high-resolution radar ranging [14]. Its key innovation lies in replacing the external LO with the transmitted signal itself to enhance system compactness. Second, RARE-based wireless communication techniques have been designed to

support a variety of modulation schemes, including amplitude, frequency, and phase modulation [15], [16]. Advances in this area have led to the development of sophisticated RARE systems [11], [17]–[20]. Notably, the concept of RARE arrays has been introduced to enable the detection of spatially multiplexed signals and pave the way for a novel paradigm termed atomic multiple-input-multiple-output (atomic-MIMO) communications [17], [18]. Additionally, RAREs have been designed to support both continuous-band and multi-band reception in broadband communication systems [11], [19], [20]. The third direction focuses on leveraging RAREs for a wide range of sensing applications. These include angle-of-arrival (AoA) estimation [21], [22], displacement detection [23], multi-band localization [24], moisture sensing [25], and integrated sensing and communication [26].

State-of-the-art RARE designs are predominantly based on the assumption that atomic vapor cells exhibit an isotropic response to incident RF fields [8], [11], [18], [19], [27]–[29]. This assumption, which is justified when the vapor cell is sufficiently short, allows the RARE to be modeled as a point receiver, thereby simplifying the input-output signal model that underpins detection and signal processing. Specifically, a signal model for LO-dressed RAREs was initially established by authors of [8] via solving the Lindblad master equation in the steady state. Subsequent studies have extended this simplified model to accommodate systems involving off-resonant optical and RF fields [19], [27], [30], as well as to enable multi-band signal reception [11]. Further advancements have generalized the steady model [8] to account for dynamic signals through Laplace transform analysis of quantum state evolution [28]. As a result of the isotropic approximation, these models often treat RAREs analogously to isotropic antennas. However, in practical scenarios, the atomic quantum states within the vapor cell typically exhibit spatial variation, especially in LO-dressed RAREs. This spatial inhomogeneity can significantly influence both the response pattern and the antenna gain of the RARE. Therefore, characterization of these spatial effects is essential for a complete understanding of RARE operation so as to fully realize their potential. However, such in-depth spatial analyses remain missing in the existing literature.

To fill in this gap, we theoretically analyze the effects of spatially varying quantum states of Rydberg atoms inside the vapor cell. Our study leads to the discovery of a previously unexplored capability of RARE, termed *single-antenna atomic beamforming*, where a directional (receive) beam is generated using a sufficiently long vapor cell with only a single pair of laser beams, a single PD, and a single LO. The main contributions are summarized below.

- **Atomic beamforming with a continuous vapor cell:**

Consider the standard RARE architecture with a continuous vapor cell. We derive a new signal model that accounts for the spatial variation of quantum states induced by the interference between the incident signal and LO fields. A key insight from this analysis is that a vapor cell with substantial length exhibits a directional reception pattern. This pattern naturally steers a beam toward the LO field direction with a beamwidth inversely proportional to the cell length, effectively realizing single-

antenna atomic beamforming. To further explore this phenomenon, we analyze the achievable beamforming gain under two noise regimes: the blackbody radiation (BBR)-limited regime and the photon shot noise (PSN)-limited regime. Our results show that, in the BBR regime, the beamforming gain increases linearly with the cell length; whereas in the PSN regime, it decays exponentially due to severe laser attenuation inside the vapor cell. This tradeoff suggests the existence of an optimal cell length that maximizes the RARE's beamforming gain.

- **Atomic beamforming with a segmental vapor cell:**

To overcome the exponential decay in beamforming gain with increasing cell length under the PSN regime, we propose a novel architecture for RAREs based on a segmental vapor cell. The key idea is to divide a continuous vapor cell into multiple cell segments with adjacent segments separated by a clear-air gap. This design allows the distribution of Rydberg atoms over an extended effective length for enhanced spatial signal reception without expanding the cell-propagation distance (and hence the light attenuation). We develop a general signal model and analyze the resulting spatial reception pattern for this architecture. Our analysis shows that a segmental vapor cell achieves narrower beamwidth and higher beamforming gain than its continuous counterpart. Moreover, the beamforming gain increases monotonically with the number of segments, avoiding the gain saturation and exponential decay observed in the case of long continuous cell.

*Organization:* The remainder of the paper is organized as follows. Section II presents the system model. The analysis of atomic beamforming with a continuous vapor cell is provided in Section III followed by beamforming analysis for the segmental vapor cell in Section IV. Numerical validations are conducted in Section V, and conclusions are drawn in Section VI.

*Notation:* Bold uppercase characters  $\mathbf{X}$  denote matrices, with  $X_{mn}$  representing its  $(m, n)$ -th entry. For two matrices  $\mathbf{A}$  and  $\mathbf{B}$ ,  $[\mathbf{A}, \mathbf{B}]$  denotes the commutator  $\mathbf{AB} - \mathbf{BA}$ , and  $\{\mathbf{A}, \mathbf{B}\}$  denotes their anti-commutator  $\mathbf{AB} + \mathbf{BA}$ .  $\langle p |$  and  $|q \rangle$  refer to the bra-ket notation.  $\mathcal{U}(a, b)$  denotes the uniform distribution over the interval  $[a, b]$ . Some default physical and mathematical constants are defined as follows:  $j = \sqrt{-1}$  the imaginary unit;  $c$  the speed of light;  $h$  the Planck constant with  $\hbar = \frac{h}{2\pi}$  its reduced form;  $\epsilon_0$  the vacuum permittivity;  $Z_0$  the vacuum impedance;  $k_B$  the Boltzmann constant; and  $q$  the elementary charge.

## II. MODELS AND METRICS

As illustrated in Fig. 1, we consider a single-antenna LO-dressed RARE system. The setup includes a pair of probe and coupling lasers for producing Rydberg atoms and a single photodetector (PD) for measuring the output probe laser signal. A continuous vapor cell of length  $L$ , filled with alkali atoms, serves as the wireless signal sensor, as detailed in Section III. This design is further extended to a segmental vapor cell architecture in Section IV. The detailed system models and performance metrics are presented below.

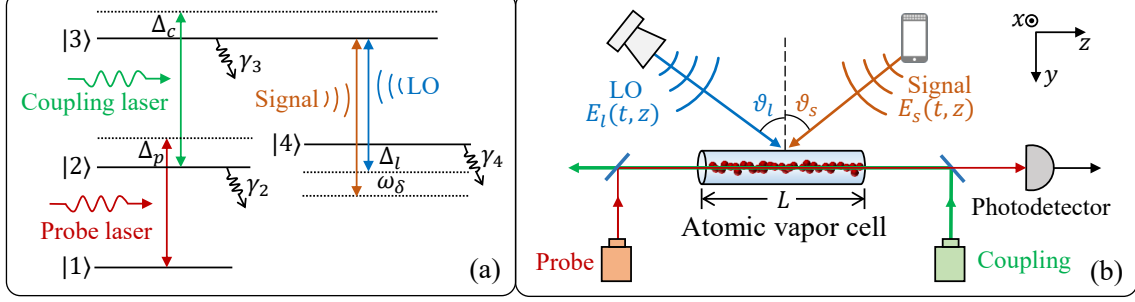


Figure 1. (a) Atomic energy levels and (b) architecture of a Rydberg atomic receiver .

### A. Electric Field Models

A RARE detects the electric field component of an incident electromagnetic wave. In the considered system, Rydberg atoms within the vapor cell are exposed to three external electric fields: the LO field \$E\_l(t, z)\$, the information-carrying signal field \$E\_s(t, z)\$, and the BBR noise field \$E\_n(t, z)\$. The total incident RF field at location \$z \in [0, L]\$ and time \$t\$ is expressed as

$$E(t, z) = E_l(t, z) + E_s(t, z) + E_n(t, z). \quad (1)$$

For simplicity, we restrict our analysis to the field component polarized along the \$x\$-axis.

We adopt the popular superheterodyne architecture [8]. The predefined LO field has a frequency slightly different from that of the signal field, resulting in a beat frequency between them. Let \$\{f\_l, \omega\_l, \lambda\_l, k\_l\}\$ and \$\{f\_s, \omega\_s, \lambda\_s, k\_s\}\$ denote the frequencies, angular frequencies, wavelengths, and wavenumbers of the LO and signal fields, respectively. The beat angular frequency is thus \$\omega\_\delta \triangleq \omega\_s - \omega\_l\$. To account for the influence of vapor-cell length on quantum response, it is essential to accurately model the spatial variations of fields. Let \$\vartheta\_l\$ and \$\vartheta\_s\$ denote the angles-of-arrival of the LO and signal fields relative to the normal direction of the vapor cell, as shown in Fig. 1(b). Under the far-field planar wavefront assumption, the fields \$E\_l(t, z)\$ and \$E\_s(t, z)\$ are modeled as

$$E_l(t, z) = E_l e^{j(\omega_l t - k_l z \theta_l + \varphi_l)}, \quad (2)$$

$$E_s(t, z) = E_s e^{j(\omega_s t - k_s z \theta_s + \varphi_s)} \stackrel{(a)}{\approx} E_s e^{j(\omega_s t - k_l z \theta_s + \varphi_s)}, \quad (3)$$

where \$E\_l > 0\$, \$\theta\_l \triangleq \sin \vartheta\_l\$, \$\varphi\_l\$ (and \$E\_s > 0\$, \$\theta\_s \triangleq \sin \vartheta\_s\$, \$\varphi\_s\$) represent the strengths, spatial directions, and phases of the LO (and signal fields). Approximation (a) holds since \$\omega\_\delta \ll \omega\_l\$. It is clear that the field models in (2) and (3) have incorporated both temporal and spatial variations of the phase profile.

For BBR field, \$E\_n(t, z)\$, we characterize it by the isotropic propagation model proposed in [31], [32]. The incident noise power is assumed to be uniformly distributed over spatial directions. By integrating the noise field over a unit spherical shell, the noise autocorrelation function is expressed as

$$\mathbb{E}[E_n(t, z)E_n^*(t', z')] = \Lambda(f_l) \text{sinc}\left(\frac{2(z-z')}{\lambda_l}\right) \delta(t-t'), \quad (4)$$

where \$\Lambda(f\_l) \triangleq \frac{2\pi Z\_0 k\_B T\_{\text{env}} f\_l^2}{c^2}\$ is the BBR spectral radiance at frequency \$f\_l\$ and environmental temperature \$T\_{\text{env}}\$ [28]. Following [31], the term \$\text{sinc}\left(\frac{2(z-z')}{\lambda\_l}\right)\$ describes the spatial

correlation of noise, where \$\text{sinc}(u) = \frac{\sin(\pi u)}{\pi u}\$ is the sinc function. Since this paper focuses on the spatial properties of atomic receivers, the temporal correlation is characterized by the impulse function \$\delta(t-t')\$ for simplicity, while extensions to general temporal correlations are straightforward.

### B. Quantum System Model

1) *Quantum state*: As depicted in Fig. 1(a), a RARE harnesses the electron transition phenomena of Rydberg atoms to sense RF signals. Alkali atoms within the vapor cell are first excited from the ground state \$|1\rangle\$ to a low-lying excited state \$|2\rangle\$ by a probe laser of angular frequency \$\omega\_p\$, then to a Rydberg state \$|3\rangle\$ using a coupling laser locked at the angular frequency \$\omega\_c\$. Such atoms can interact strongly with the incident field, \$E(t, z)\$, further inducing the electron transition \$|3\rangle \rightarrow |4\rangle\$. In this four-level quantum system, the quantum state is described by a \$4 \times 4\$ density matrix:

$$\rho = \sum_{p=1}^4 \sum_{q=1}^4 \rho_{pq} |p\rangle \langle q| \in \mathbb{C}^{4 \times 4}. \quad (5)$$

2) *Quantum state evolution*: The evolution of quantum states is governed by the Lindblad master equation [8]:

$$\frac{\partial \rho}{\partial t} = -\frac{j}{\hbar} [\mathbf{H}, \rho] + \mathcal{L}. \quad (6)$$

In this equation, \$\mathcal{L}\$ represents the decoherence operator resulting from the spontaneous emission, which is written as \$\mathcal{L} = -\frac{1}{2}\{\Gamma, \rho\} + \Lambda\$. Here, \$\Gamma = \text{diag}\{0, \gamma\_2, \gamma\_3, \gamma\_4\}\$, \$\Lambda = \text{diag}\{\gamma\_2 \rho\_{22} + \gamma\_4 \rho\_{44}, \gamma\_3 \rho\_{33}, 0, 0\}\$, and \$\gamma\_i\$, \$i = 2, 3, 4\$ are the spontaneous decay rates of the \$i\$-th level. The Hamiltonian operator \$\mathbf{H} \in \mathbb{C}^{4 \times 4}\$ in the rotating frame is given by

$$\mathbf{H} = \hbar \begin{bmatrix} 0 & \frac{\Omega_p}{2} & 0 & 0 \\ \frac{\Omega_p}{2} & -\Delta_p & \frac{\Omega_c}{2} & 0 \\ 0 & \frac{\Omega_c}{2} & -\Delta_p - \Delta_c & \frac{\Omega_l + \Omega_s^* + \Omega_n^*}{2} \\ 0 & 0 & \frac{\Omega_l + \Omega_s + \Omega_n}{2} & -\Delta_p - \Delta_c - \Delta_l \end{bmatrix}, \quad (7)$$

where \$\Delta\_p \triangleq \omega\_p - \omega\_{12}\$, \$\Delta\_c \triangleq \omega\_c - \omega\_{23}\$, and \$\Delta\_l \triangleq \omega\_l - \omega\_{34}\$ are the frequency detunings from resonance, where \$\omega\_{pq}\$ refers to the transition frequency of \$|p\rangle \rightarrow |q\rangle\$. \$\Omega\_p\$, \$\Omega\_c\$, \$\Omega\_l\$, \$\Omega\_s\$, and \$\Omega\_n\$ denote Rabi frequencies of the probe, coupling, LO, signal, and the BBR fields, respectively, which are associated with the intensity of the resonant electron transition. Note that \$\Omega\_p\$, \$\Omega\_c\$, and \$\Omega\_l\$ are usually modeled as positive real values due to the monochromatic configuration [8]. Rabi frequencies \$\Omega\_s\$ and \$\Omega\_n\$ are complex functions of time \$t\$ and location \$z\$ due

to the presence of the beat frequency and spatial variation of the phase profile. By setting the phase of the LO field as a baseline, we have [33]

$$\begin{cases} \Omega_l = \frac{\mu_{34}}{\hbar} E_l \\ \Omega_s = \frac{\mu_{34}}{\hbar} E_s(t, z) e^{-j\angle E_l(t, z)} \stackrel{(a)}{=} \frac{\mu_{34}}{\hbar} E_s e^{j(\omega_\delta t - k_l z \theta_\delta + \varphi_\delta)} \\ \Omega_n = \frac{\mu_{34}}{\hbar} E_n(t, z) e^{-j\angle E_l(t, z)} \stackrel{(b)}{=} \frac{\mu_{34}}{\hbar} E_n(t, z) e^{j k_l z \theta_l} \end{cases}, \quad (8)$$

where  $\mu_{34}$  is the transition dipole moment between  $|3\rangle$  and  $|4\rangle$ . In (a), we define  $\theta_\delta \triangleq \theta_s - \theta_l$  as the difference of spatial directions between LO and signal fields and  $\varphi_\delta \triangleq \varphi_s - \varphi_l$  as the phase difference. In (b), the phase  $(\omega_l t + \varphi_l)$  is absorbed in the noise  $E_n(t, z)$ . For ease of future usage, we define the Rabi frequency amplitude of the total electric field as

$$\Omega(t, z) \triangleq |\Omega_l + \Omega_s(t, z) + \Omega_n(t, z)|. \quad (9)$$

3) *Transmissive probe laser*: We are interested in the solution of the (1, 2)-th entry of  $\rho$ , i.e.,  $\rho_{12}$ , as it is associated with the probe laser to be measured. Existing studies have proposed diverse approaches to derive  $\rho_{12}$  under various conditions [8], [11], [19], [27]. It is well established that  $\rho_{12}$  depends on the signal field  $E_s(t, z)$  via the Rabi frequency amplitude:

$$\rho_{12} = \rho_{12}(\Omega(t, z)) = \rho_{12}(|\Omega_l + \Omega_s(t, z) + \Omega_n(t, z)|). \quad (10)$$

The subsequent analysis relies solely on this relationship, while the explicit functional form of  $\rho_{12}$  is unnecessary. Moreover, due to atomic thermal motion, lasers illuminating the atoms experience a random Doppler shift. Consequently, the observed quantum state  $\rho_{12}$  should be averaged over all possible shifts as follows [34]:

$$\bar{\rho}_{12} = \int_{-\infty}^{+\infty} \frac{e^{-v^2/u^2}}{\sqrt{\pi}u} \rho_{12} \left( \Delta_p - \frac{2\pi v}{\lambda_p}, \Delta_c + \frac{2\pi v}{\lambda_c} \right) dv, \quad (11)$$

where  $u \triangleq \sqrt{k_B T_{\text{env}}/m}$  with  $m$  being the atom's mass. Here,  $\frac{2\pi v}{\lambda_p}$  and  $\frac{2\pi v}{\lambda_c}$  denote the Doppler shifts of the probe and coupling lasers for atoms at velocity  $v$ .

As the probe laser passes through the vapor cell, its output power is determined by the quantum state  $\bar{\rho}_{12}$ . Denote the power of the probe laser at the input of the vapor cell as  $P_{\text{in}}$ . In accordance with the Bouguer-Beer-Lambert law, the transmissive probe-laser power is expressed as

$$P_{\text{out}}(t) = P_{\text{in}} e^{-\int_0^L \chi(\Omega(t, z)) dz}. \quad (12)$$

The amplitude attenuation coefficient,  $\chi(\Omega(t, z))$ , characterizes the susceptibility of the vapor cell to the probe laser at position  $z$  and time  $t$ . It is related to the Doppler-averaged quantum state as follows [8]:

$$\chi(\Omega(t, z)) = -\frac{k_p N_0 \mu_{12}^2}{\epsilon_0 \hbar \Omega_p} \text{Im}(\bar{\rho}_{12}(\Omega(t, z))), \quad (13)$$

where  $k_p$  is the wavelength of the probe laser,  $N_0$  the atomic density, and  $\mu_{12}$  the transition dipole moment from  $|1\rangle$  to  $|2\rangle$ .

4) *Quantum measurement model*: For performing quantum measurement, a RARE uses a PD to capture the probe laser and transduce it into photocurrent [33]:

$$\begin{aligned} I(t) &= \frac{q\eta}{\hbar\omega_p} P_{\text{out}}(t) + \Delta I_{\text{psn}}(t) \\ &= I_{\text{in}} e^{-\int_0^L \chi(\Omega(t, z)) dz} + \Delta I_{\text{psn}}(t), \end{aligned} \quad (14)$$

Here,  $\eta$  is the quantum efficiency of the PD and  $\Delta I_{\text{psn}}(t)$  denotes the PSN. The notation of equivalent input current,  $I_{\text{in}} \triangleq \frac{q\eta P_{\text{in}}}{\hbar\omega_p}$ , is introduced to ease the expression.

In state-of-the-art RAREs, the LO field is typically much stronger than the signal and BBR fields  $\Omega_l \gg |\Omega_{s,n}(t, z)|$ . Using first-order Taylor expansion, this strong LO configuration yields the decomposition of the measured photocurrent [14]:

$$I(t) = \underbrace{\bar{I}}_{\text{Zero order}} + \underbrace{\Delta I_s(t) + \Delta I_{\text{bbr}}(t)}_{\text{First order}} + \Delta I_{\text{psn}}(t). \quad (15)$$

The zero-order current  $\bar{I}$  is a time-invariant direct-current (DC) bias arising from the strong LO field  $E_l(t, z)$ ; the time-oscillating currents  $\Delta I_s(t)$  and  $\Delta I_{\text{bbr}}(t)$  are associated with the information-carrying signal field  $E_s(t, z)$  and the BBR field  $E_n(t, z)$ , respectively. The rationale of (15) and explicit expressions of  $\bar{I}$ ,  $\Delta I_s(t)$ ,  $\Delta I_{\text{bbr}}(t)$ ,  $\Delta I_{\text{psn}}(t)$  will be discussed in subsequent sections. Without causing any confusion, we will term  $\Delta I_s(t)$  as “signal” and  $\Delta I_{\text{bbr}}(t)$  as “BBR noise” in the following discussions.

### C. Signal-to-Noise Ratio

We use the SNR metric to evaluate the sensitivity of a RARE. Consider a time window of  $T_s = \frac{2n\pi}{\omega_s}$ ,  $n \in \mathbb{Z}^+$  for performing match-filter detection. Assume  $T_s$  is sufficiently long such that the power spectra of noise components  $\Delta I_{\text{bbr}}(t)$  and  $\Delta I_{\text{psn}}(t)$  within bandwidth  $B_s = \frac{1}{T_s}$  are white. In this context, the SNR can be expressed as

$$\text{SNR} = \frac{\mathcal{P}_s}{\mathcal{N}_{\text{bbr}} + \mathcal{N}_{\text{psn}}}, \quad (16)$$

where  $\mathcal{P}_s$  denotes the accumulated energy of the signal:

$$\mathcal{P}_s = \int_0^{T_s} \Delta I_s^2(t) dt. \quad (17)$$

The power density of the BBR noise  $\mathcal{N}_{\text{bbr}}$  is given by the time integral of its correlation function:

$$\mathcal{N}_{\text{bbr}} = \int_0^{T_s} \mathcal{R}_{\text{bbr}}(\tau) d\tau, \quad (18)$$

where  $\mathcal{R}_{\text{bbr}}(\tau) \triangleq \mathbb{E}[\Delta I_{\text{bbr}}(t) \Delta I_{\text{bbr}}(t + \tau)]$  is the correlation function. According to [28], the power density associated with the PSN  $\Delta I_{\text{psn}}(t)$  is related to the DC bias as

$$\mathcal{N}_{\text{psn}} = q\bar{I}. \quad (19)$$

$$\begin{aligned}
I(t) &= I_{\text{in}} e^{-\int_0^L \chi(\Omega(t,z)) dz} + \Delta I_{\text{psn}}(t) \approx I_{\text{in}} e^{-\int_0^L \chi_l dz} e^{-\int_0^L \dot{\chi}_l \text{Re}\{\Omega_s(t,z) + \Omega_n(t,z)\} dz} + \Delta I_{\text{psn}}(t) \\
&\stackrel{(a)}{\approx} \underbrace{I_{\text{in}} e^{-\chi_l L}}_{\bar{I}} \underbrace{- I_{\text{in}} e^{-\chi_l L} \dot{\chi}_l \frac{\mu_{34}}{\hbar} \int_0^L \text{Re}\{E_s(t,z) e^{-j\angle E_l(t,z)}\} dz}_{\Delta I_s(t)} \underbrace{- I_{\text{in}} e^{-\chi_l L} \dot{\chi}_l \int_0^L \text{Re}\{\Omega_n(t,z)\} dz + \Delta I_{\text{psn}}(t)}_{\Delta I_{\text{bbr}}(t)}. \quad (21)
\end{aligned}$$

#### D. A Myth and Reality

1) *Myth*: In the analysis of the characteristics of a RARE, previous research often adopts the *point receiver* approximation [8], [11], [19], [27], [28]. Specifically, the length of the vapor cell,  $L$ , is assumed to be sufficiently short such that the quantum state  $\bar{\rho}_{12}(\Omega(t,z))$  is considered spatially invariant, i.e.  $\bar{\rho}_{12}(\Omega(t,z)) = \bar{\rho}_{12}(\Omega(t,0))$ . This assumption simplifies the transmissive probe-laser power as  $P_{\text{out}}(t) = P_{\text{in}} e^{-L\chi(\Omega(t,0))}$ . Under this assumption, closed-form expressions of the signal energy  $\mathcal{P}_s$ , noise energy  $\mathcal{N}_{\text{bbr}} + \mathcal{N}_{\text{psn}}$ , and SNR are derived, and the conclusion that RAREs behave as *isotropic quantum antennas* is obtained [18], [29].

2) *Reality*: However, the point receiver assumption neglects the spatial variation of the quantum state  $\bar{\rho}_{12}(\Omega(t,z))$  along the vapor cell, which results from the spatially varying phase,  $k_l z \theta_\delta$ , of the Rabi frequency. Particularly, when the vapor cell is long, this omission can result in inaccurate modeling of the probe-laser power and the associated SNR, leading to misunderstandings regarding the characteristics of a practical RARE. The theme of the next section is to correct this misunderstanding.

### III. ATOMIC BEAMFORMING WITH A CONTINUOUS VAPOR CELL

Building upon the preceding “myth and reality” discussion, this section presents a key finding: the consideration of spatially varying quantum states within a continuous vapor cell results in the formation of a receive-beam. To support this, generalized signal and noise models for RARE are derived, incorporating spatially varying quantum states. Our analysis demonstrates that RAREs exhibit isotropic quantum antenna behavior only when the vapor cell is sufficiently short. In contrast, long vapor cells exhibit directional reception patterns, enabling *single-antenna atomic beamforming*.

#### A. Mathematical Characterization of Signal, Noise, and SNR

To establish comprehensive signal and noise models, it is essential to derive a closed-form expression for the photocurrent decomposition in (15). On the strong LO condition,  $\Omega_l \gg |\Omega_{s,n}(t,z)|$ , the susceptibility at position  $z$  and  $t$  can be linearized as

$$\begin{aligned}
\chi(\Omega(t,z)) &\approx \chi(\Omega_l) + \frac{d\chi}{d\Omega_l} \text{Re}\{\Omega_s(t,z) + \Omega_n(t,z)\} \quad (20) \\
&= \chi_l + \dot{\chi}_l \frac{\mu_{34}}{\hbar} \text{Re}\{E_s(t,z) e^{-j\angle E_l(t,z)} + E_n(t,z) e^{-j\angle E_l(t,z)}\}.
\end{aligned}$$

The zero-order term  $\chi_l \triangleq \chi(\Omega_l)$  and first derivative term  $\dot{\chi}_l \triangleq \frac{d\chi}{d\Omega_l}$  depend solely on the spatially-invariant LO’s Rabi frequency,  $\Omega_l$ . Substituting (20) into (12) yields the photocurrent decomposition in (21), where approximation (a)

follows from the Taylor expansion  $e^{-x} = 1 - x + \mathcal{O}(x^2)$ . This decomposition facilitates the calculation of the time-oscillating signal  $\Delta I_s$  and noise components  $\Delta I_{\text{bbr}}$  and  $\Delta I_{\text{psn}}$ , as well as their respective energy.

1) *Signal characterization*: By calculating the integral in (21), the information-bearing signal current is derived as

$$\begin{aligned}
\Delta I_s(t) &= -I_{\text{in}} e^{-\chi_l L} \dot{\chi}_l \frac{\mu_{34}}{\hbar} \int_0^L \text{Re}\{E_s(t,z) e^{-j\angle E_l(t,z)}\} dz \\
&= \underbrace{-I_{\text{in}} e^{-\chi_l L} L \text{sinc}\left(\frac{L\theta_\delta}{\lambda_l}\right) \dot{\chi}_l \frac{\mu_{34}}{\hbar} E_s \cos(\omega_\delta t + \varphi'_\delta)}_{\text{Intrinsic gain } \kappa(\theta_\delta)}, \quad (22)
\end{aligned}$$

where  $\varphi'_\delta = \varphi_\delta - \frac{\pi L \theta_\delta}{\lambda_l}$ . The integral in (22) reveals that an atomic vapor cell is equivalent to a continuous phased array of length  $L$ , rather than a single phase shifter as interpreted in existing studies [8], [35]. The resultant signal current is proportional to the aggregation of phase-shifted signal fields along the vapor cell, where the phase shifts are provided by the spatial phase profile of the LO field,  $\angle E_l(t,z)$ . Due to the configuration of the planar wavefront, the integral naturally results in the dependence of the intrinsic gain  $\kappa(\theta_\delta)$  on the incident direction via the sinc function term  $\text{sinc}\left(\frac{L\theta_\delta}{\lambda_l}\right)$ . As we will discuss later, this dependence fundamentally distinguishes the long-cell behavior from short-cell properties.

The energy of  $\Delta I_s(t)$  follows from integrating  $\Delta I_s^2(t)$  over the time window  $T_s = \frac{2\pi\omega_\delta}{\omega_\delta}, \forall n \in \mathbb{Z}^+$ :

$$\mathcal{P}_s = \frac{1}{2} \kappa^2(\theta_\delta) E_s^2 T_s. \quad (23)$$

2) *Noise characterization*: Given the integral form of BBR noise  $\Delta I_{\text{bbr}}(t)$  in (21), the correlation function,  $\mathcal{R}_{\text{bbr}}(\tau)$ , is shown to be (see Appendix A)

$$\mathcal{R}_{\text{bbr}}(\tau) = \frac{1}{2} I_{\text{in}}^2 e^{-2\chi_l L} \xi\left(\frac{L}{\lambda_l}; \theta_\delta\right) \lambda_l^2 \dot{\chi}_l^2 \frac{\mu_{34}^2}{\hbar^2} \Lambda(f_l) \delta(\tau), \quad (24)$$

where  $\xi(d; \theta_\delta) \triangleq \int_{-d}^d (d - |u|) \text{sinc}(2u) \cos(2\pi\theta_\delta u) du$ . The noise power density is thus obtained as

$$\mathcal{N}_{\text{bbr}} = \frac{1}{2} I_{\text{in}}^2 e^{-2\chi_l L} \xi\left(\frac{L}{\lambda_l}; \theta_\delta\right) \lambda_l^2 \dot{\chi}_l^2 \frac{\mu_{34}^2}{\hbar^2} \Lambda(f_l). \quad (25)$$

In terms of the PSN, given the DC bias of  $\bar{I} = I_{\text{in}} e^{-\chi_l L}$ , the power density is

$$\mathcal{N}_{\text{psn}} = q I_{\text{in}} e^{-\chi_l L}. \quad (26)$$

3) *SNR characterization*: By combining (23)-(26), the measured SNR at the PD is formulated as

$$\text{SNR} = \frac{\text{sinc}^2\left(\frac{L\theta_\delta}{\lambda_l}\right) L^2 e^{-\chi_l L} E_s^2 T_s}{\xi\left(\frac{L}{\lambda_l}; \theta_\delta\right) \lambda_l^2 e^{-\chi_l L} \Lambda(f_l) + \beta_l}, \quad (27)$$

where  $\beta_l \triangleq \frac{2\hbar^2 q}{I_{\text{in}}\mu_{34}^2\chi_l^2}$  is a constant that describes the relative strength of PSN. Equation (27) reveals a critical dependence of SNR on the cell length,  $L$ , and spatial directions,  $\theta_l$  and  $\theta_s$ , indicating a spatial pattern of the single-antenna RARE. In the following, we analyze this spatial pattern by examining the asymptotic SNRs for both short- and long-vapor-cell cases.

### B. Short Vapor Cell as an Isotropic Quantum Antenna

Existing literature mainly focuses on the short-vapor-cell scenario with  $L \ll \lambda_l$  and ignores the effects of cell length  $L$ . This subsection revisits this analysis and provides a comprehensive discussion to the influence of cell length  $L$  on the SNR, reception pattern, and aperture.

1) *Asymptotic SNR*: When  $L \ll \lambda_l$ , we find that  $\lim_{L/\lambda_l \rightarrow 0} \text{sinc}(L\theta_\delta/\lambda_l) = 1$  and

$$\xi\left(\frac{L}{\lambda_l}; \theta_l\right) \simeq \int_{-\frac{L}{\lambda_l}}^{\frac{L}{\lambda_l}} \left(\frac{L}{\lambda_l} - |u|\right) du = \frac{L^2}{\lambda_l^2}. \quad (28)$$

By substituting (28) into (27), the SNR is asymptotically

$$\text{SNR} \simeq \frac{L^2 e^{-\chi_l L} E_s^2 T_s}{L^2 e^{-\chi_l L} \Lambda(f_l) + \beta_l}, \quad (29)$$

2) *Isotropic reception pattern*: In this short-cell limit, the SNR becomes independent of the spatial directions  $\theta_s$  of signal and  $\theta_l$  of LO. This results in a uniform SNR observed by the PD, regardless of the incident directions of electric fields, demonstrating an isotropic quantum antenna behavior.

3) *Atomic antenna aperture*: Another finding of interest from (29) is that both signal field intensity,  $E_s^2$ , and BBR field strength,  $\Lambda(f_l)$ , experience an equivalent scaling of

$$A_q = L^2 e^{-\chi_l L} \quad (30)$$

in the unit of area.

Analogous to the definition of classical antenna aperture,  $A_q$  can be interpreted as the *atomic aperture* of this small quantum antenna. Unlike classical counterparts, the atomic aperture  $L^2 e^{-\chi_l L}$  exhibits a tradeoff as regulated by the cell length  $L$ . For sufficiently small  $L$ , the limited number of participating Rydberg atoms results in reduced sensitivity to external electric fields, thereby decreasing atomic aperture. Conversely, for longer vapor cells (yet still smaller than  $\lambda_l$ ), exponential attenuation of the probe laser along the vapor cell diminishes sensitivity, also leading to a reduced atomic aperture. Hence, an intermediate vapor cell length is preferred to maximize the atomic aperture. By setting the derivative of  $A_q(L)$  to 0, the optimal vapor cell length is found to be

$$L^* = 2/\chi_l, \quad (31)$$

yielding the *largest atomic aperture* of

$$A_q^* = 4/(e^2 \chi_l^2). \quad (32)$$

In existing implementations of RARE, the amplitude attenuation coefficient  $\chi_l$  typically ranges from  $0.25 \text{ cm}^{-1}$  to  $2 \text{ cm}^{-1}$ . This corresponds to a range of optimal length  $L^* \in [1 \text{ cm}, 8 \text{ cm}]$  and that of the largest atomic aperture  $A_q^* \in [0.135 \text{ cm}^2, 8.66 \text{ cm}^2]$ . It is important to emphasize that

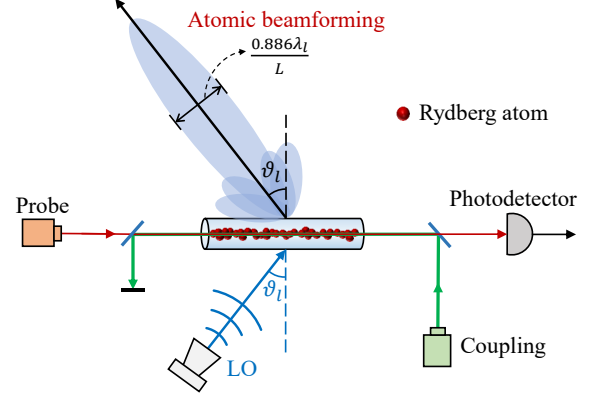


Figure 2. Long vapor cell as an atomic beamformer.

the optimality of (31) holds when  $L \ll \lambda_l$ . Given a longest length of 8 cm, our analysis of optimal atomic aperture is applicable to frequency bands lower than  $\sim 3 \text{ GHz}$ .

### C. Long Vapor Cell as an Atomic Beamformer

Turn now to the long-cell scenario where  $L \gg \lambda_l$ . This scenario is common at high-frequency bands, such as the midband (7-24 GHz) and mmWave band (30-300 GHz). In this context, the influence of the sinc function inside  $\mathcal{P}_s$  on the SNR can no longer be ignored, and the BBR noise's power density  $\mathcal{N}_{\text{bb}}^2$  requires correction.

1) *Asymptotic SNR*: Specifically, as  $\frac{L}{\lambda_l} \rightarrow +\infty$ , the function  $\xi\left(\frac{L}{\lambda_l}; \theta_l\right)$  is asymptotically

$$\xi\left(\frac{L}{\lambda_l}; \theta_l\right) \simeq \frac{L}{\lambda_l} \int_{-\infty}^{\infty} \text{sinc}(2u) \cos(2\pi\theta_l u) du \stackrel{(a)}{=} \frac{L}{2\lambda_l}. \quad (33)$$

The proof of (a) is straightforward by performing Fourier transform on  $\text{sinc}(2u)$ . Comparing (28) and (33), one can observe that the function  $\xi\left(\frac{L}{\lambda_l}; \theta_l\right)$  that characterizes the BBR's power density is no longer quadratically related to  $\frac{L}{\lambda_l}$  but linearly. This order reduction arises because the BBR fields between two positions become less correlated as their distance increases. As a result, the asymptotic SNR is expressed as

$$\text{SNR} \simeq \text{sinc}^2\left(\frac{L\theta_\delta}{\lambda_l}\right) \frac{L^2 e^{-\chi_l L} E_s^2 T_s}{\frac{1}{2} L \lambda_l e^{-\chi_l L} \Lambda(f_l) + \beta_l}. \quad (34)$$

2) *Receive beamforming pattern*: One can observe from (34) that the measured SNR for a long vapor cell exhibits dependence on the incident spatial directions  $\theta_l$  and  $\theta_s$ . This dependence results in a directional reception pattern of the long vapor cell:

$$G(\theta_\delta) = \frac{\mathcal{P}_s(\theta_\delta)}{\mathcal{P}_{s,\text{max}}} = \text{sinc}^2\left(\frac{L\theta_\delta}{\lambda_l}\right), \quad (35)$$

where  $\mathcal{P}_{s,\text{max}}$  is achieved at  $\theta_\delta = 0$ . High SNR is observed only when the incident signal field's direction  $\theta_s$  closely aligns with the LO field's direction  $\theta_l$ . In contrast, when the deviation  $\theta_\delta$  is large, the antenna pattern severely suppresses the signal field, resulting in a low SNR. As illustrated in Fig. 2, this directional reception pattern effectively forms a beam centered at  $\theta_l$ , rendering the RARE with a long vapor cell no longer an isotropic antenna but an atomic beamformer.

The half-power beamwidth (HPBW), which quantifies the directivity, can be calculated from the equation  $\text{sinc}^2\left(\frac{L\theta_\delta}{\lambda_l}\right) = \frac{1}{2}$  with  $\theta_{\text{HPBW}} = 2\theta_\delta$ . The result gives the HPBW as follows:

$$\theta_{\text{HPBW}} = 0.886 \frac{\lambda_l}{L} [\text{Rad}]. \quad (36)$$

Clearly, a longer cell length gives a narrower beamwidth.

**Remark 1** (Key features of atomic beamformer). Some key features of the atomic beamformer are summarized as follows.

- **Single-antenna beamforming capability:** The discovered beamforming capability requires only a single quantum antenna equipped with a sufficiently long vapor cell, a single pair of probe and coupling lasers, a single PD for measurement, and a LO for direction control. This single-antenna system can be regarded as a quantum analogue of the traditional analog beamforming architecture, where the PD functions similarly to a conventional analog-to-digital converter, and the vapor cell corresponds to a continuous phased array with phase shifts provided by the LO field.
- **Low hardware cost:** Vapor cells can be much more cost-effective than similarly sized phased arrays. As frequency increases, the number of antennas needed to achieve the same array aperture in traditional phased arrays scales linearly, necessitating complex RF circuit designs [36]. In contrast, the intrinsic nature of continuous phased arrays for atomic vapor cells eliminates the need for RF circuits, enabling operation across all frequency bands without hardware modifications.
- **Beam direction control:** The beamforming direction is determined by the incident angle of the LO field, as shown in Fig. 2. To adaptively steer the beam, the LO source can be mounted on a circular rail connected to a motor, allowing for mechanical rotation of the LO's direction  $\theta_l$ .

3) *Atomic beamforming gain:* To gain deeper insights into the fundamental limits of atomic beamforming gain, we analyze the scaling law of the SNR. Two regimes are considered: the BBR regime  $\text{SNR}_{\text{bbbr}} = \frac{P_s}{N_{\text{bbbr}}}$  and the PSN regime  $\text{SNR}_{\text{psn}} = \frac{P_s}{N_{\text{psn}}}$ . The former describes an external-noise-limited scenario in which BBR noise dominates, while the latter pertains to a PSN-limited scenario. The total SNR can be obtained from these two regimes:

$$\text{SNR} = \frac{\text{SNR}_{\text{bbbr}} \text{SNR}_{\text{psn}}}{\text{SNR}_{\text{bbbr}} + \text{SNR}_{\text{psn}}}. \quad (37)$$

i) *Beamforming gain for aligned  $\theta_s$  and  $\theta_l$ :* By assuming a perfect alignment between the incident directions of the LO and signal fields ( $\theta_s = \theta_l$ ), we have  $\text{sinc}^2\left(\frac{L\theta_\delta}{\lambda_l}\right) = 1$ . Then, SNRs under the BBR and PSN regimes become

$$\begin{cases} \text{SNR}_{\text{bbbr}} \simeq \frac{2LE_s^2T_s}{\lambda_l\Lambda(f_l)} = \mathcal{O}\left(\frac{L}{\lambda_l}\right) \\ \text{SNR}_{\text{psn}} \simeq \frac{L^2e^{-\chi_l L}E_s^2T_s}{\beta_l} = \mathcal{O}\left(L^2e^{-\chi_l L}\right) \end{cases}. \quad (38)$$

In the BBR regime, the beamforming gain is proportional to  $\frac{L}{\lambda_l}$ , which is analogous to that of a classic phased array.

This gain arises because the signal fields along the vapor cell are coherently aggregated at the PD, while the BBR field's aggregation is incoherent for large  $\frac{L}{\lambda_l}$ , as explained in (33). Thereby, a longer vapor cell is preferred to mitigate the BBR. In the PSN regime, the SNR grows linearly with the atomic aperture  $A_q = L^2e^{-\chi_l L}$ . This relationship comes because the signal field intensity  $E_s^2$  is amplified by  $L^2e^{-2\chi_l L}$ , while the internal PSN  $N_{\text{psn}}$  is proportional to the DC bias  $\bar{P}_{\text{out}} \propto e^{-\chi_l L}$ . Their ratio precisely yields the atomic aperture.

**Remark 2** (Tradeoff between BBR and PSN regimes). While the BBR regime suggests an unbounded growth of SNR as the cell length increases, the PSN regime prevents this infinite growth. As  $L \rightarrow +\infty$ , although  $\text{SNR}_{\text{bbbr}}$  linearly improves, the energy of signal  $P_s$  and BBR noise  $N_{\text{bbbr}}$  decays exponentially faster than the PSN's energy  $N_{\text{psn}}$ . Consequently, the system quickly transitions into the PSN regime, resulting in an exponential decline of the SNR. Thereafter, similar to the short-cell configuration, an optimal vapor cell length exists that maximizes the SNR, leaving room for cell-length optimization.

ii) *Beamforming gain outside the HPBW:* We further examine the achieved beamforming gain at undesired directions that are outside the HPBW:  $|\theta_\delta| > \theta_{\text{HPBW}}$ . Given the upper bound of the sinc function  $\text{sinc}^2\left(\frac{L\theta_\delta}{\lambda_l}\right) \leq \frac{\lambda_l^2}{L^2\theta_\delta^2}$ , SNRs in the two regimes are upper-bounded by

$$\begin{cases} \text{SNR}_{\text{bbbr}} \lesssim \frac{2\lambda_l E_s^2 T_s}{\pi^2 \theta_\delta^2 L \Lambda(f_l)} = \mathcal{O}\left(\frac{\lambda_l}{L\theta_\delta^2}\right) \\ \text{SNR}_{\text{psn}} \lesssim \frac{\lambda_l^2 e^{-\chi_l L} E_s^2 T_s}{\pi^2 \theta_\delta^2 \beta_l} = \mathcal{O}\left(\frac{\lambda_l^2}{\theta_\delta^2 e^{\chi_l L}}\right) \end{cases}. \quad (39)$$

For both the BBR and PSN regimes, the upper bounds of SNRs decline quadratically with respect to the direction deviation  $\theta_\delta$ . Linearly-decaying and exponentially-decaying SNRs as the increasing cell length  $L$  are observed for the BBR and PSN regimes, respectively. These findings indicate that a longer vapor cell can consistently narrow the HPBW and suppress the received SNR of signals outside the HPBW, re-verifying the beamforming capability of the single-antenna RARE. Leveraging this property, interference mitigation and spatial-division multiple access can be potentially achieved.

#### IV. ATOMIC BEAMFORMING WITH A SEGMENTAL VAPOR CELL

There is a drawback associated with atomic beamforming using a continuous vapor cell. Although increasing the cell length,  $L$ , can narrow the beamwidth, the beamforming gain does not improve monotonically. Instead, the gain ultimately declines in the PSN regime due to the exponential decay of laser power within the vapor cell. This limitation constrains the overall beamforming performance. In this section, we propose an alternative architecture for the single-antenna RARE system—the segmental vapor cell—to mitigate this issue, as illustrated in Fig. 3. The key idea is to uniformly divide the standard continuous cell of length  $L$  into  $M$  smaller segments. These segments are aligned in a line with a clear-air gap,  $d_g$ , separating each adjacency. This architecture allows for the expansion of the effectively occupied length of all segments by increasing either the number of segments,  $M$ , or the gap,

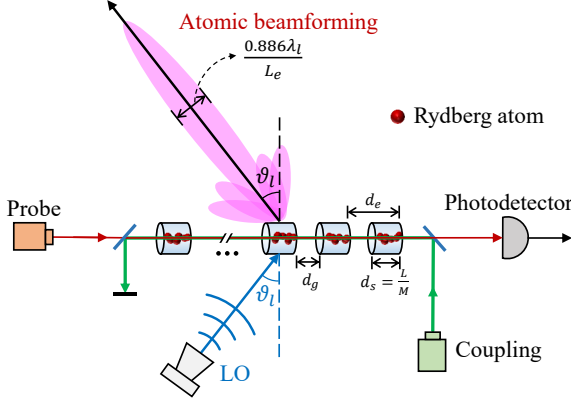


Figure 3. Architecture of a segmental vapor cell.

$d_g$ , without increasing the attenuation distance of light,  $L$ . It can thereby provide a narrower beamwidth and higher beamforming gain than the continuous-cell architecture.

#### A. Mathematical Characterization of Signal, Noise, and SNR

We provide a mathematical characterization of the received signals and noises with a segmental vapor cell. A single pair of laser beams simultaneously passes through the entire array of cell segments, while the probe laser is detected by a single PD. Denote the length and effectively occupied length of each segment as  $d_s = \frac{L}{M}$  and  $d_e = d_s + d_g$ , respectively. The overall effective length occupied by all segments is thus enlarged to  $L_e = L + (M-1)d_g$ . Consider the fact that the reflection coefficient of commercial anti-reflection (AR) coated vapor cells is less than 0.5% [37], and the atmospheric attenuation coefficient of light in a clear environment is less than 1dB/km [38]. The reflection losses at cell surfaces and the free-space attenuation can be safely neglected. As a result, the total decay experienced by the probe laser is approximated by replacing the attenuation within a continuous cell (as in (12)) with a sum of attenuation over all segments:

$$P_{\text{in}} e^{-\int_0^L \chi(\Omega(t, z)) dz} \Rightarrow P_{\text{in}} e^{-\sum_{m=0}^{M-1} \int_{m d_e}^{(m+1) d_e} \chi(\Omega(t, z)) dz}.$$

By applying the strong LO approximation in (20), the photocurrent measured at the PD can be decomposed as in (40). Based on (40), we can analyze the received signal  $\Delta I_s(t)$  and BBR noise  $\Delta I_{\text{bbr}}(t)$  in the sequel.

1) *Signal characterization:* By calculating the sum of integrals in (40), the signal component of photocurrent follows

$$\begin{aligned} \Delta I_s(t) = & \underbrace{-I_{\text{in}} e^{-\chi_l L} L \text{sinc} \left( \frac{d_s \theta_\delta}{\lambda_l} \right) \Xi_M \left( \frac{d_e \theta_\delta}{\lambda_l} \right) \dot{\chi}_l \frac{\mu_{34}^2}{\hbar}}_{\text{Intrinsic gain } \kappa(\theta_\delta)} \\ & \times E_s \cos(\omega_\delta t + \varphi_\delta''), \end{aligned} \quad (41)$$

where  $\Xi_M(x) \triangleq \frac{\sin(M\pi x)}{M \sin(\pi x)}$  refers to the Dirichlet sinc function, and  $\varphi_\delta'' = \varphi_\delta - \frac{\pi d_s \theta_\delta}{\lambda_l} - \frac{\pi(M-1)d\theta_\delta}{\lambda_l}$ . The accumulated energy over the time window  $T_s = \frac{2\pi}{\omega_\delta}$ ,  $\forall n \in \mathbb{Z}^+$  is thus

$$\mathcal{P}_s = \frac{1}{2} \kappa^2(\theta_\delta) E_s^2 T_s. \quad (42)$$

It is clear from (41) and (42) that the reception pattern of a segmental vapor cell is determined by the product of  $\text{sinc}^2 \left( \frac{d_s \theta_\delta}{\lambda_l} \right)$  and  $\Xi_M^2 \left( \frac{d_e \theta_\delta}{\lambda_l} \right)$ . The resultant pattern of

$$G(\theta_\delta) = \frac{\mathcal{P}_s(\theta_\delta)}{\mathcal{P}_{s,\text{max}}} = \text{sinc}^2 \left( \frac{d_s \theta_\delta}{\lambda_l} \right) \Xi_M^2 \left( \frac{d_e \theta_\delta}{\lambda_l} \right) \quad (43)$$

reflects the principle of pattern multiplication in classic antenna theory [39]. Particularly, the sinc term, arising from the continuous integral of fields within each segment, characterizes the antenna pattern of an individual cell segment. The latter Dirichlet sinc term stems from the discrete summation of fields across all cell segments, describing the antenna pattern of the entire segment array.

Analogous to the scenario of a long continuous cell, a beam steered towards the LO's direction  $\theta_s = \theta_l$  is formed by the segmental cell, as depicted in Fig. 3. Note that the HPBW in this setting is largely determined by the antenna pattern  $\Xi_M^2 \left( \frac{d_e \theta_\delta}{\lambda_l} \right)$ . This is because the effectively occupied length of all segments  $L_e = L + (M-1)d_g \approx L + M d_g = M d_e$  is much longer than one segment's length,  $d_s = \frac{L}{M}$ , when the number of segments is large. Solving the equation  $\Xi_M^2 \left( \frac{d_e \theta_\delta}{\lambda_l} \right) = \frac{1}{2}$  with  $\theta_{\text{HPBW}} = 2\theta_\delta$ , we obtain the HPBW as follows:

$$\theta_{\text{HPBW}} = 0.886 \frac{\lambda_l}{M d_e} \approx 0.886 \frac{\lambda_l}{L_e} [\text{Rad}]. \quad (44)$$

**Remark 3** (Narrower beamwidth). It is clear from (36) and (44) that the HPBW of a segmental vapor cell is no longer determined by the overall cell length,  $L$ , but by the overall effective length,  $L_e = L + (M-1)d_g$ . Due to the introduced clear-air gap,  $d_g$ , the HPBW of a segmental cell is narrower than that of a continuous cell. Moreover, a narrower beamwidth can be achieved by either increasing the number of cell segments,  $M$ , or by enlarging the gap,  $d_g$ , without increasing the cell length  $L$ .

2) *Noise characterization:* Since DC bias  $\bar{I}$  remains unchanged, the PSN's power density of a segmental vapor cell is identical to that of a continuous vapor cell. As for the BBR noise, we assume that BBR fields at different cell segments are uncorrelated for ease of discussion. Then, the new correlation function is derived as (see Appendix B)

$$\mathcal{R}_{\text{bbr}}(\tau) = \frac{1}{2} I_{\text{in}}^2 e^{-2\chi_l L} M \xi \left( \frac{d_s}{\lambda_l}; \theta_l \right) \lambda_l^2 \dot{\chi}_l^2 \frac{\mu_{34}^2}{\hbar^2} \Lambda(f_l) \delta(\tau), \quad (45)$$

which results in the BBR noise's power density:

$$\mathcal{N}_{\text{bbr}} = \frac{1}{2} I_{\text{in}}^2 e^{-2\chi_l L} M \xi \left( \frac{d_s}{\lambda_l}; \theta_l \right) \lambda_l^2 \dot{\chi}_l^2 \frac{\mu_{34}^2}{\hbar^2} \Lambda(f_l). \quad (46)$$

3) *SNR characterization:* Combining (42)-(46) yields the formulation of SNR observed at the PD:

$$\text{SNR} = \frac{\text{sinc}^2 \left( \frac{d_s \theta_\delta}{\lambda_l} \right) \Xi_M^2 \left( \frac{d_e \theta_\delta}{\lambda_l} \right) L^2 e^{-\chi_l L} E_s^2 T_s}{M \xi \left( \frac{d_s}{\lambda_l}; \theta_l \right) \lambda_l^2 e^{-\chi_l L} \Lambda(f_l) + \beta_l}. \quad (47)$$

In the following subsections, we analyze the achievable beamforming gain of a segmental vapor cell by examining the asymptotic SNRs under both short- and long-segment settings.

$$\begin{aligned}
I(t) &= I_{\text{in}} e^{-\sum_{m=0}^{M-1} \int_{md_e}^{md_e+d_s} \chi(\Omega(t,z)) dz} + \Delta I_{\text{psn}}(t) \approx I_{\text{in}} e^{-\chi_l L} e^{-\sum_{m=0}^{M-1} \int_{md_e}^{md_e+d_s} \dot{\chi}_l \operatorname{Re}\{\Omega_s(t,z) + \Omega_n(t,z)\} dz} + \Delta I_{\text{psn}}(t) \\
&\approx \underbrace{I_{\text{in}} e^{-\chi_l L}}_{\bar{I}} - \underbrace{I_{\text{in}} e^{-\chi_l L} \dot{\chi}_l \sum_{m=0}^{M-1} \int_{md_e}^{md_e+d_s} \operatorname{Re}\{\Omega_s(t,z)\} dz - I_{\text{in}} e^{-\chi_l L} \dot{\chi}_l \sum_{m=0}^{M-1} \int_{md_e}^{md_e+d_s} \operatorname{Re}\{\Omega_n(t,z)\} dz}_{\Delta I_s(t)} + \underbrace{\Delta I_{\text{psn}}(t)}_{\Delta I_{\text{bbr}}(t)}. \quad (40)
\end{aligned}$$

### B. Beamforming Gain with Short Cell Segments

1) *Asymptotic SNR*: Consider the case of small cell segments at first, where the length of each cell segment is much shorter than the wavelength  $d_s \ll \lambda_l$ . As we have proved in Section III-B, the function  $\xi\left(\frac{d_s}{\lambda_l}; \theta_l\right)$  is asymptotically  $\xi\left(\frac{d_s}{\lambda_l}; \theta_l\right) \simeq \frac{d_s^2}{\lambda_l^2}$ , which gives the asymptotic SNR of

$$\text{SNR} \simeq \frac{\operatorname{sinc}^2\left(\frac{d_s \theta_\delta}{\lambda_l}\right) \Xi_M^2\left(\frac{d_s \theta_\delta}{\lambda_l}\right) L^2 e^{-\chi_l L} E_s^2 T_s}{\frac{1}{M} L^2 e^{-\chi_l L} \Lambda(f_l) + \beta_l}. \quad (48)$$

2) *Atomic beamforming gain*: Based on the derived SNR in (48), we can examine the beamforming gains under the BBR and PSN regimes, respectively. Assuming the beam direction  $\theta_l$  is perfectly aligned with the signal detection  $\theta_s$ , the SNRs under the two regimes are derived as

$$\begin{cases} \text{SNR}_{\text{bbr}} \simeq \frac{M E_s^2 T_s}{\Lambda(f_l)} = \mathcal{O}(M) \\ \text{SNR}_{\text{psn}} \simeq \frac{L^2 e^{-\chi_l L} E_s^2 T_s}{\beta_l} = \mathcal{O}(L^2 e^{-\chi_l L}) \end{cases}. \quad (49)$$

Some insights can be drawn from (49). First, as BBR fields between different cell segments are uncorrelated, the BBR noise's power density is reduced by a factor of  $\frac{1}{M}$  compared with that of a continuous short cell, as derived in (29). Therefore, a beamforming gain on the order of  $\mathcal{O}(M)$  is achieved in the BBR regime. Moreover, since the segmental-vapor-cell architecture does not alter the overall cell length  $L$ , the measured energy of signal and PSN remains identical to those of a continuous cell. Henceforth, the SNR in the PSN regime remains unchanged, keeping linearly related to the atomic aperture  $A_q = L^2 e^{-\chi_l L}$  and is independent of the number of segments  $M$ . Combining these observations, we summarize the characteristics of beamforming gain as follows.

**Remark 4** (Beamforming gain with short cell segments). Increasing the number of segments,  $M$ , allows for a continuous enhancement of the beamforming gain. As  $M$  increases, the total SNR improves monotonically, in contrast to the case of a continuous vapor cell, where the SNR initially increases but eventually decays exponentially with the cell length  $L$ . Ultimately, the total SNR approaches an upper bound determined by the PSN regime  $\text{SNR}_{\text{psn}}$ . This upper bound can be independently optimized through appropriate selection of the cell length  $L$ .

### C. Beamforming Gain with Long Cell Segments

1) *Asymptotic SNR*: Now consider the scenario of long segments, where the length of each cell segment significantly exceeds the wavelength, i.e.,  $d_s \gg \lambda_l$ . This setting differs from a short segment primarily in the power density of the

BBR noise. As shown earlier, when  $\frac{d_s}{\lambda_l} \rightarrow +\infty$ , we have  $\xi\left(\frac{d_s}{\lambda_l}; \theta_l\right) \simeq \frac{d_s}{2\lambda_l}$ . Thus, the asymptotic SNR is derived as

$$\text{SNR} \simeq \frac{\operatorname{sinc}^2\left(\frac{d_s \theta_\delta}{\lambda_l}\right) \Xi_M^2\left(\frac{d_s \theta_\delta}{\lambda_l}\right) L^2 e^{-\chi_l L} E_s^2 T_s}{\frac{1}{2} L \lambda_l e^{-\chi_l L} \Lambda(f_l) + \beta_l}. \quad (50)$$

2) *Atomic beamforming gain*: Following previous discussions, when  $\theta_s = \theta_l$ , SNRs in the BBR and PSN regimes can be simplified from (50) as

$$\begin{cases} \text{SNR}_{\text{bbr}} \simeq \frac{2 L E_s^2 T_s}{\lambda_l \Lambda(f_l)} = \mathcal{O}\left(\frac{L}{\lambda_l}\right) \\ \text{SNR}_{\text{psn}} \simeq \frac{L^2 e^{-\chi_l L} E_s^2 T_s}{\beta_l} = \mathcal{O}(L^2 e^{-\chi_l L}) \end{cases}. \quad (51)$$

It is noteworthy that the asymptotic behavior of SNRs for long cell segments mirrors that of a long continuous vapor cell. This equivalence stems from two reasons. First, maintaining a fixed cell length,  $L$ , preserves the energy of signal and PSN,  $\mathcal{P}_s$  and  $\mathcal{N}_{\text{psn}}$ , captured by the sensor. Second, since each segment's length,  $d_s$ , is large, the BBR field within a cell segment exhibits a comparable amount of correlation to that within a continuous cell of length  $L$ , leading to the same BBR noise intensity  $\mathcal{N}_{\text{bbr}}$ . Based on these observations, we provide some characteristics of beamforming gain as follows.

**Remark 5** (Beamforming gain with long cell segments). As the number of cell segments  $M$  increases, the beamwidth, given by  $\frac{0.886 \lambda_l}{M d_e}$ , becomes narrower. However, this does not result in a significant increase in beamforming gain, as the signal and noise intensities remain unchanged. This situation persists until  $M$  becomes sufficiently large such that each cell segment's length  $d_s = \frac{L}{M}$  falls below the wavelength  $\lambda_l$ . Under this condition, the asymptotic SNR is expected to obey the scaling law of a short segment in (49).

## V. NUMERICAL VALIDATION

In this section, we present numerical validation for the single-antenna atomic beamforming. The default simulation settings are as follows unless specified otherwise. The RARE employs Cesium-133 atomic vapor cells with an atomic density of  $N_0 = 4.89 \times 10^{10} \text{ cm}^{-3}$ . The four energy levels are  $6S_{1/2}$ ,  $6P_{3/2}$ ,  $48D_{5/2}$ , and  $49P_{3/2}$ . The decay rates are aligned with the values in [8]. Vapor cells are illuminated by a probe laser at 852 nm with a Rabi frequency of  $\Omega_p = 2\pi \times 5.7 \text{ MHz}$  and an input power of  $P_{\text{in}} = 120 \mu\text{W}$ , and a coupling laser at 509 nm with a Rabi frequency of  $2\pi \times 0.89 \text{ MHz}$  and an input power of 40 mW to trigger the electron transitions  $|1\rangle \rightarrow |2\rangle \rightarrow |3\rangle$ . The LO has a carrier frequency of  $f_l = 6.9458 \text{ GHz}$  and an incident field strength of  $E_l = 34.6 \text{ mV/m}$  to trigger the transition

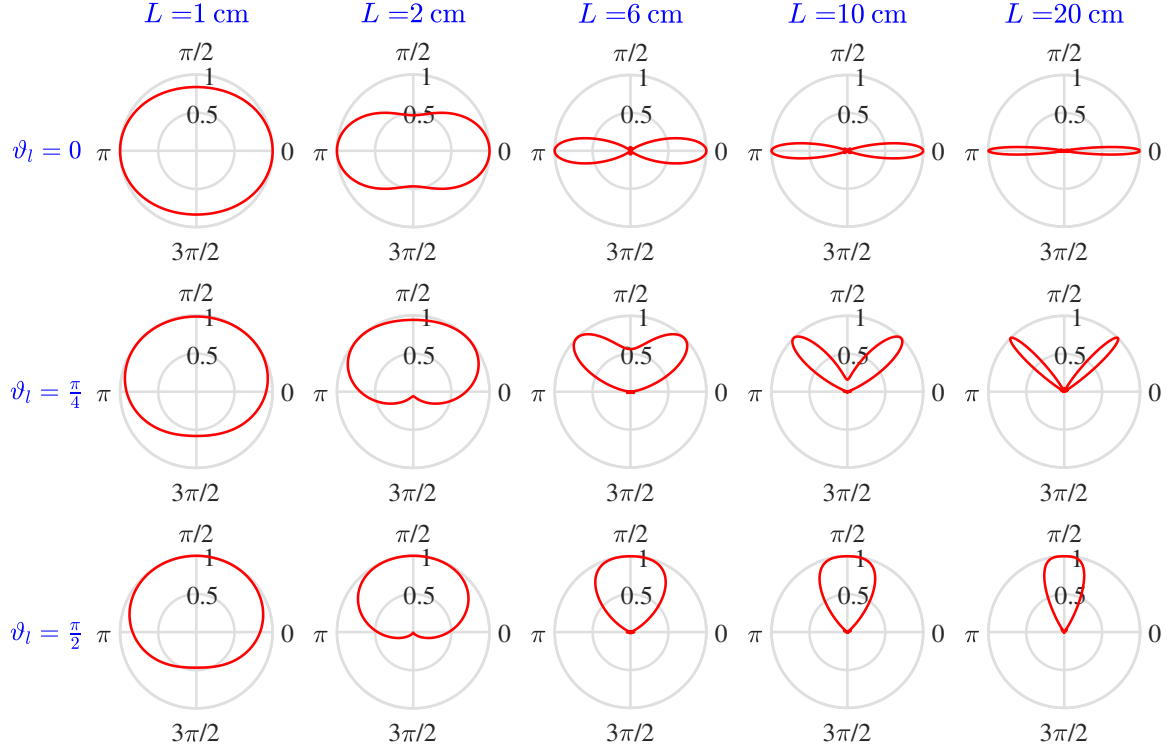
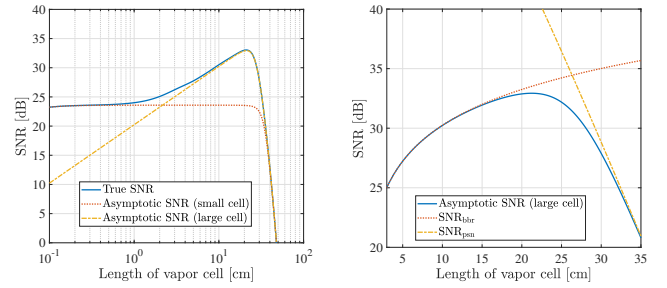


Figure 4. Antenna patterns of continuous vapor cells. The LO's incident directions are set as  $0$ ,  $\frac{\pi}{4}$ , and  $\frac{\pi}{2}$ , and the cell length grows from  $1$  cm to  $20$  cm.

$|3\rangle \rightarrow |4\rangle$ . Under this configuration, the susceptibility and its gradient are numerically obtained as  $\chi_l = 42.4 \text{ m}^{-1}$  and  $\dot{\chi}_l = 2.08 \times 10^{-5} \text{ m}^{-1} \text{ Hz}^{-1}$ . The field strength of the incident signal field is set to  $E_s = 154.9 \mu\text{V/m}$ . The frequency difference and time window are configured as  $\omega_\delta = 2\pi \times 100 \text{ kHz}$  and  $T_s = 10 \mu\text{s}$ , respectively. All noise sources are exposed to an environmental temperature at  $T_{\text{env}} = 290$  Kelvin. The quantum efficiency is  $\eta = 0.8$ .

#### A. Atomic Beamforming with a Continuous Vapor Cell

We first evaluate the beamforming performance of continuous vapor cells. The antenna patterns with different LO directions and cell lengths are illustrated in Fig. 4. The LO fields originate from three directions:  $\vartheta_l = 0$ ,  $\vartheta_l = \frac{\pi}{4}$ , and  $\vartheta_l = \frac{\pi}{2}$ , and the cell length varies from  $L = 1$  cm to  $L = 20$  cm. Since the wavelength is  $\lambda_l = 4.32$  cm, Fig. 4 encompasses both short-cell and long-cell scenarios. Key findings are summarized below. First, the atomic vapor cell behaves as an isotropic antenna when the cell length is small. Specifically, at  $L = 1$  cm, the HPBW is nearly  $2\pi$ , and no null points are observed in the antenna pattern. This aligns with existing literature indicating that a RARE exhibits an isotropic reception pattern [18], [29]. Conversely, as the cell length increases, the HPBW of the atomic antenna pattern continuously narrows, resulting in a sharp spatial selectivity. For example, increasing  $L$  from  $6$  cm to  $20$  cm reduces the HPBW approximately from  $36^\circ$  to  $11^\circ$ . Additionally, the beam direction is governed by the incident direction of the LO field. Therefore, beam steering can be accomplished with a single-antenna RARE by mechanically adjusting the position and orientation of the LO source.



(a) SNRs for short and long cells (b) SNRs in BBR and PSN regimes  
Figure 5. Influence of length,  $L$ , of a continuous vapor cell on SNR. (a) Evaluations of asymptotic SNRs for short and long cells. (b) Evaluations of SNRs in BBR and PSN regimes.

Fig. 5 evaluates the influence of cell length  $L$  on the received SNR. In Fig. 5(a), the true SNR in (27), and the asymptotic SNRs for short cells in (29), and long cells in (34), are examined. In Fig. 5(b), asymptotic SNRs for long cells within the BBR and PSN regimes, as shown in (38), are compared. As observed in Fig. 5(a), the asymptotic behaviors of SNR align closely with the accurate values in both short and long cell limits. The intersection point of these two limits is approximately  $L = 1 \sim 2$  cm. Moreover, as  $L$  increases, the SNR initially rises and suddenly falls. This behavior can be interpreted by the tradeoff between BBR and PSN regimes, as illustrated in Fig. 5(b). In the BBR regime, increasing  $L$  from  $3$  cm to  $22$  cm results in an SNR improvement from approximately  $25$  dB to  $33$  dB. This is attributed to the beamforming gain of  $\mathcal{O}(L)$  achieved by long cells. In contrast, for  $L > 25$  cm, the PSN regime dominates, and the SNR decreases exponentially owing to the severe laser attenuation. As a result, to maximize SNR, selecting an intermediate cell

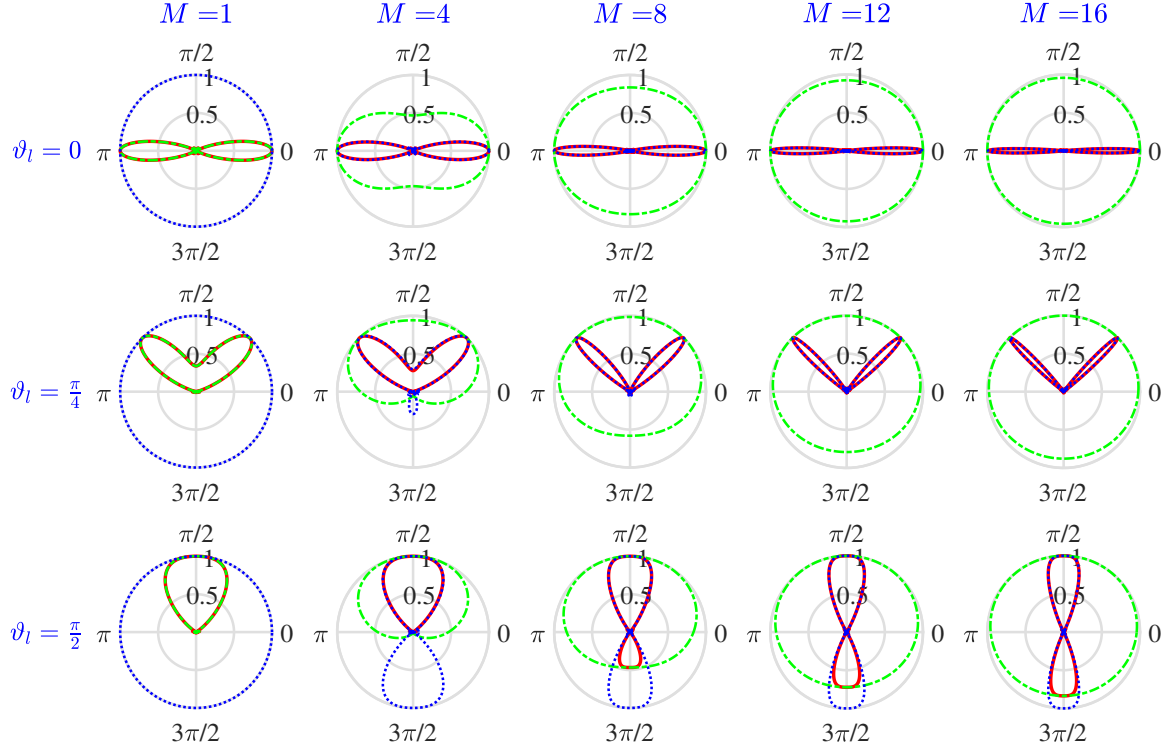


Figure 6. Antenna patterns of segmental vapor cells. The LO's incident directions are set as  $0$ ,  $\frac{\pi}{4}$ , and  $\frac{\pi}{2}$ , the cell length is fixed as  $L = 8$  cm, and the number of segments increases from 1 to 16.

length near the intersection point of these regimes, around  $L = 22$  cm, is recommended for practical implementations of atomic vapor cells.

### B. Atomic Beamforming with a Segmental Vapor Cell

In this subsection, the beamforming performance achieved by segmental vapor cells is numerically validated. Fig. 6 illustrates the generated beam pattern with different numbers of segments,  $M$ . For all sub-figures, the overall cell length,  $L$ , is fixed at 8cm. Except for the case where  $M = 1$ , the effective length of each segment is set to  $d_e = \frac{\lambda_l}{2} = 2.16$ cm. The dotted curves in green and blue depict the patterns of a cell segment,  $\text{sinc}^2\left(\frac{d_s \theta_\delta}{\lambda_l}\right)$ , and the entire segment array,  $\Xi_M^2\left(\frac{d_e \theta_\delta}{\lambda_l}\right)$ , respectively. The red curve characterizes the produced pattern  $\text{sinc}^2\left(\frac{d_s \theta_\delta}{\lambda_l}\right) \Xi_M^2\left(\frac{d_e \theta_\delta}{\lambda_l}\right)$ . As shown in Fig. 6, the increment in the number of segments continuously narrows the beamwidth, despite the fixed cell dimension  $L$ . This effect is attributed to the increased effective aperture of the all cell segments. Another notable observation is the presence of a back lobe when  $\theta_l = \frac{\pi}{2}$  and  $M > 8$ , a phenomenon not observed in the continuous-cell configuration. This back lobe results from the discrete nature of segmental vapor cells. Specifically, at  $\theta_l = \frac{\pi}{2}$ , the pattern of the segment array,  $\Xi_M^2\left(\frac{d_e \theta_\delta}{\lambda_l}\right)$ , inherently exhibits a back lobe, as indicated by the blue curves in the last row. For a small number of segments, each cell segment's length  $d_s = L/M$  is sufficiently large, allowing for the suppression of back lobes by the individual segment's antenna pattern  $\text{sinc}^2\left(\frac{d_s \theta_\delta}{\lambda_l}\right)$ . Conversely, for a large  $M$  and correspondingly a small segment length  $d_s = L/M$ , each cell segment behaves like an isotropic antenna, resulting in an inability to suppress the back lobe.

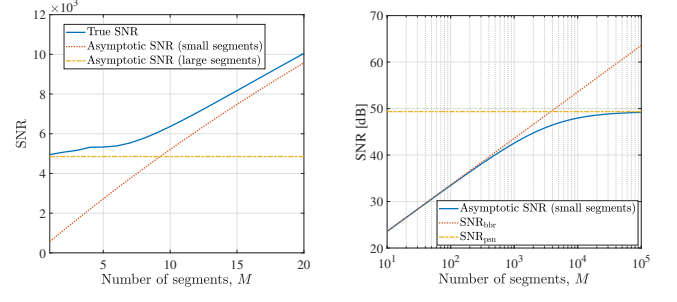


Figure 7. Influence of the numbers of segments,  $M$ , on SNRs. (a) Evaluations of asymptotic SNRs for short and long cells. (b) Evaluations of SNRs in BBR and PSN regimes.

Fig. 7 presents the numerical results of SNR with different numbers of segments. Sub-figures (a) and (b) correspond to small-scale and large-scale settings, respectively, with  $M \in [1, 20]$  and  $M \in [10, 10^5]$ . Focusing first on sub-figure (a), the curves depict the true SNR in (47), together with asymptotic SNRs with short segments in (48) and with long segments in (50). The overall cell length is fixed at  $L = 20$  cm, with a clear-air gap of  $d_g = 1$ cm. These results align with the insights discussed in **Remarks 4-5**. Specifically, for a small number of segments ( $M < 7$ ), the received SNR remains approximately constant as  $M$  increases, indicating no additional beamforming gain due to the large segment length  $d_s = \frac{L}{M}$ . Conversely, as  $M$  exceeds approximately 10, the segment length becomes sufficiently short. Then, the SNR grows linearly with  $M$ , demonstrating a beamforming gain of  $\mathcal{O}(M)$ . Sub-figure (b) examines the asymptotic SNRs in the limit of large  $M$ , within the BBR and PSN regimes. The overall cell length is fixed

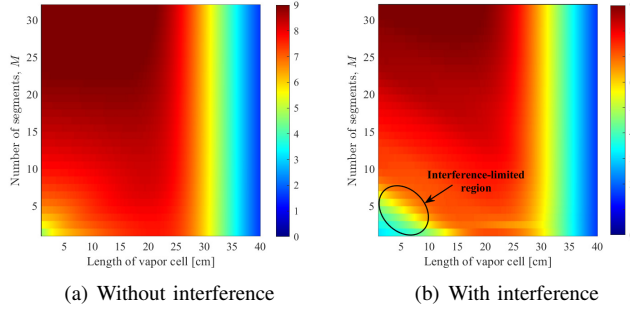


Figure 8. Channel capacities as functions of the number of segments and the cell length under conditions (a) without and (b) with interference.

at  $L = 10$  cm, and the effective area of each cell segment is  $d_e = \frac{\lambda_l}{2} = 2.16$  cm. The achieved SNR monotonically grows with respect to  $M$  and ultimately converges to the upper bound set by  $\text{SNR}_{\text{psn}}$ . More than 20 dB enhancement in SNR is achieved when  $M$  increases from  $10^1$  to  $10^4$ . Noteworthy, the issue of exponentially-decaying  $\text{SNR}_{\text{psn}}$  has been effectively addressed as the beamforming gain is reaped by increasing the number of segments rather than the cell length  $L$ . These results validate the superiority of the proposed segmental-vapor-cell architecture in enhancing beamforming performance.

### C. Channel Capacity

To demonstrate the interference mitigation capability of single-antenna atomic beamforming, we show channel capacities as functions of the number of segments ( $M \in [1, 32]$ ) and the cell length ( $L \in [1 \text{ cm}, 40 \text{ cm}]$ ) in Fig. 8. The channel capacity in the presence of interference is given by

$$C = \log_2 \left( 1 + \frac{\mathcal{P}_s}{\mathcal{P}_I + \mathcal{N}_{\text{bbr}} + \mathcal{N}_{\text{psn}}} \right) \quad [\text{bit/s/Hz}], \quad (53)$$

where  $\mathcal{P}_I$  denotes the interference energy. In our simulation,  $\mathcal{P}_I$  has a similar form to  $\mathcal{P}_s$ , except for differing incident direction  $\theta_i = \sin \vartheta_i$  and field strength  $E_i$ . We assume identical directions for the signal and LO fields, with  $\vartheta_l = \vartheta_s = \frac{\pi}{4}$ . Subfigure (a) depicts an ideal interference-free scenario with  $E_i = 0$ , while subfigure (b) assumes that the interference originates from a random direction:  $\vartheta_i \sim \mathcal{U}(-\frac{\pi}{2}, \frac{\pi}{2})$  with a random strength  $E_i \sim \mathcal{U}(0, \frac{1}{2}E_s)$ . 1000 Monte-Carlo simulations are carried out to plot each figure. At short cell lengths (e.g.,  $L < 10$  cm) and small numbers of segments (e.g.,

$M < 7$ ), the generated beam is broad, leading to a significant interference. Consequently, the channel capacity decreases by approximately 3 bits compared with the ideal interference-free case. However, with a large number of segments (e.g.,  $M > 20$ ) and an intermediate cell length (e.g.,  $L = 20$  cm), the interference is effectively suppressed by the pencil-like beam pattern, yielding channel capacities comparable to the interference-free scenario. These results highlight the potential of atomic beamforming for interference mitigation.

## VI. CONCLUSIONS

This paper has reported the new finding that a RARE has the capability of single-antenna atomic beamforming. We demonstrated that long cells form a distinct beam pattern with a beamwidth inversely proportional to the cell length. The fundamental tradeoff of beamforming gain in BBR and PSN regimes was revealed. A novel architecture of segmental vapor cell was introduced to overcome the exponential gain decay in the PSN regime. Numerical results demonstrated a 7 dB SNR enhancement by optimizing cell length, a 20 dB SNR improvement by implementing a segmental architecture, and an interference mitigation capability of atomic beamforming.

This work discovers a neglected physical phenomenon of RAREs, i.e., single-antenna atomic beamforming. This phenomenon opens several promising avenues for future research. One direction involves advancing atomic beam management techniques, including the quantum analogue of beam sweeping and beam tracking. Another is the design of atomic multi-antenna beamforming with multiple laser beams and multiple PDs to support orthogonal multiple access.

## APPENDIX

### A. Proof of (24)

Adopting the form of  $\Delta I_{\text{bbr}}(t)$  in (21), the correlation function  $\mathcal{R}_{\text{bbr}}(\tau)$  is derived in (52). Here, (a) arises from the correlation function of the BBR field in (4), (b) holds because of the integral by substitution:  $u = z - z'$  and  $v = z + z'$ , and (c) comes from the definition  $\xi(d; \theta_l) \triangleq \int_{-d}^d (d - |u|) \text{sinc}(2u) \cos(2\pi\theta_l u) du$ . This completes the proof.

### B. Proof of (46)

Similar to the proof of (24), the derivation of BBR noise correlation function is presented in (54). Here, (a) arises because the BBR fields among different cells are uncorrelated.

$$\begin{aligned} \mathcal{R}_{\text{bbr}}(\tau) &= \left( I_{\text{in}} e^{-\chi_l L} \dot{\chi}_l \frac{\mu_{34}}{\hbar} \right)^2 \int_0^L \int_0^L \mathbb{E}(\text{Re}\{E_n(t, z) e^{j k_l z \theta_l}\} \text{Re}\{E_n(t + \tau, z') e^{j k_l z' \theta_l}\}) dz dz' \\ &= \frac{1}{2} \left( I_{\text{in}} e^{-\chi_l L} \dot{\chi}_l \frac{\mu_{34}}{\hbar} \right)^2 \int_0^L \int_0^L \text{Re}\left\{ \mathbb{E}(E_n(t, z) E_n^*(t + \tau, z') e^{j k_l (z - z') \theta_l}) \right\} dz dz' \\ &\stackrel{(a)}{=} \frac{1}{2} \left( I_{\text{in}} e^{-\chi_l L} \dot{\chi}_l \frac{\mu_{34}}{\hbar} \right)^2 \Lambda(f_l) \delta(\tau) \int_0^L \int_0^L \text{sinc}(2(z - z')/\lambda_l) \cos(2\pi(z - z')\theta_l/\lambda_l) dz dz' \\ &\stackrel{(b)}{=} \frac{1}{2} \left( I_{\text{in}} e^{-\chi_l L} \dot{\chi}_l \frac{\mu_{34}}{\hbar} \right)^2 \Lambda(f_l) \delta(\tau) \int_{-L}^L (L - |u|) \text{sinc}(2u/\lambda_l) \cos(2\pi\theta_l u/\lambda_l) du \\ &\stackrel{(c)}{=} \frac{1}{2} I_{\text{in}}^2 e^{-2\chi_l L} \xi\left(\frac{L}{\lambda_l}; \theta_l\right) \lambda_l^2 \dot{\chi}_l^2 \frac{\mu_{34}^2}{\hbar^2} \Lambda(f_l) \delta(\tau). \end{aligned} \quad (52)$$

$$\begin{aligned}
\mathcal{R}_{\text{bb}}(\tau) &= \left( I_{\text{in}} e^{-\chi_l L} \dot{\chi}_l \frac{\mu_{34}}{\hbar} \right)^2 \sum_{m, m'} \int_{m d_e}^{m d_e + d_s} \int_{m' d_e}^{m' d_e + d_s} \mathbb{E}(\text{Re}\{E_n(t, z) e^{j k_l z \theta_l}\} \text{Re}\{E_n(t, z') e^{j k_l z' \theta_l}\}) dz dz' \\
&\stackrel{(a)}{=} \sum_m \frac{1}{2} \left( I_{\text{in}} e^{-\chi_l L} \dot{\chi}_l \frac{\mu_{34}}{\hbar} \right)^2 \int_{m d_e}^{m d_e + d_s} \int_{m d_e}^{m d_e + d_s} \text{Re}\{\mathbb{E}(E_n(t, z) E_n^*(t, z')) e^{j k_l (z - z') \theta_l}\} dz dz' \\
&= \sum_m \frac{1}{2} \left( I_{\text{in}} e^{-\chi_l L} \dot{\chi}_l \frac{\mu_{34}}{\hbar} \right)^2 \Lambda(f_l) \lambda_l^2 \int_{-d_s/\lambda_l}^{d_s/\lambda_l} (d_s/\lambda_l - |u|) \text{sinc}(2u) \cos(2\pi\theta_l u) \delta(\tau) du \\
&= \frac{1}{2} I_{\text{in}}^2 e^{-2\chi_l L} M \xi \left( \frac{d_s}{\lambda_l}; \theta_l \right) \lambda_l^2 \dot{\chi}_l^2 \frac{\mu_{34}^2}{\hbar^2} \Lambda(f_l) \delta(\tau).
\end{aligned} \tag{54}$$

## REFERENCES

- [1] L. Hanzo, Z. Babar, Z. Cai, D. Chandra, I. B. Djordjevic, B. Koczor, S. X. Ng, M. Razavi, and O. Simeone, "Quantum information processing, sensing, and communications: Their myths, realities, and futures," *Proc. IEEE*, pp. 1–51, 2025.
- [2] C. L. Degen, F. Reinhard, and P. Cappellaro, "Quantum sensing," *Rev. Mod. Phys.*, vol. 89, p. 035002, Jul. 2017.
- [3] Z. Zhang and Q. Zhuang, "Distributed quantum sensing," *Quantum Sci. Technol.*, vol. 6, no. 4, p. 043001, jul 2021.
- [4] M. Cui, Q. Zeng, and K. Huang, "Rydberg atomic receiver: Next frontier of wireless communications," *IEEE Commun. Mag.*, 2025.
- [5] H. Fan, S. Kumar, J. Sedlacek, H. Kübler, S. Karimkashi, and J. P. Shaffer, "Atom based RF electric field sensing," *J. Phys. B: At. Mol. Opt. Phys.*, vol. 48, no. 20, p. 202001, Sep. 2015.
- [6] J. A. Sedlacek, A. Schwettmann, H. Kübler, R. Löw, T. Pfau, and J. P. Shaffer, "Microwave electrometry with Rydberg atoms in a vapour cell using bright atomic resonances," *Nat. Phys.*, vol. 8, no. 11, pp. 819–824, Nov. 2012.
- [7] H. Nyquist, "Thermal agitation of electric charge in conductors," *Phys. Rev.*, vol. 32, no. 1, pp. 110–113, Jul. 1928.
- [8] M. Jing, Y. H. Hu, J. Ma, H. Zhang, L. Zhang, L. Xiao, and S. Jia, "Atomic superheterodyne receiver based on microwave-dressed Rydberg spectroscopy," *Nat. Phys.*, vol. 1, pp. 911–915, Jun. 2020.
- [9] G. Sandige, G. Santamaria-Botello, E. Bottomley, H. Fan, and Z. Popović, "Resonant structures for sensitivity enhancement of Rydberg-atom microwave receivers," *IEEE Trans. Microw. Theory Techn.*, vol. 72, no. 4, pp. 2057–2066, Apr. 2024.
- [10] L. Li, Y. Jiao, J. Hu, H. Li, M. Shi, J. Zhao, and S. Jia, "Super low-frequency electric field measurement based on rydberg atoms," *Opt. Express*, vol. 31, no. 18, pp. 29 228–29 234, Aug. 2023.
- [11] M. Cui, Q. Zeng, Z. Wang, and K. Huang, "Rydberg atomic receivers for multi-band communications and sensing," *arXiv preprint arXiv:2505.24168*, May 2025.
- [12] J. A. Gordon, C. L. Holloway, S. Jefferts, and T. Heavner, "Quantum-based si traceable electric-field probe," in *Proc. 2010 IEEE Int'l Symp. Electro. Compat.*, 2010, pp. 321–324.
- [13] M. Cai, S. You, S. Zhang, Z. Xu, and H. Liu, "Sensitivity extension of atom-based amplitude-modulation microwave electrometry via high Rydberg states," *Appl. Phys. Lett.*, vol. 122, no. 16, p. 161103, Apr. 2023.
- [14] M. Cui, Q. Zeng, Z. Wang, and K. Huang, "Realizing quantum wireless sensing without extra reference sources: Architecture, algorithm, and sensitivity maximization," *arXiv preprint arXiv:2504.21234*, Apr. 2025.
- [15] D. H. Meyer, K. C. Cox, F. K. Fatemi, and P. D. Kunz, "Digital communication with Rydberg atoms and amplitude-modulated microwave fields," *Appl. Phys. Lett.*, vol. 112, no. 21, p. 211108, May 2018.
- [16] M. T. Simons, A. H. Haddab, J. A. Gordon, and C. L. Holloway, "A Rydberg atom-based mixer: Measuring the phase of a radio frequency wave," *Appl. Phys. Lett.*, vol. 114, no. 11, p. 114101, Mar. 2019.
- [17] M. Cui, Q. Zeng, and K. Huang, "Towards atomic MIMO receivers," *IEEE J. Sel. Areas Commun.*, vol. 43, no. 3, pp. 659–673, Jan. 2025.
- [18] S. S. A. Yuan, X. Y. I. Xu, J. Yuan, G. Xie, C. Huang, X. Chen, Z. Huang, and W. E. I. Sha, "Electromagnetic modeling and capacity analysis of Rydberg atom-based MIMO system," *IEEE Antennas Wireless Propag. Lett.*, vol. 24, no. 7, pp. 1839–1843, Jul. 2025.
- [19] X.-H. Liu, K.-Y. Liao, Z.-X. Zhang, H.-T. Tu, W. Bian, Z.-Q. Li, S.-Y. Zheng, H.-H. Li, W. Huang, H. Yan, and S.-L. Zhu, "Continuous-frequency microwave heterodyne detection in an atomic vapor cell," *Phys. Rev. Appl.*, vol. 18, no. 5, p. 054003, Nov. 2022.
- [20] Y. Du, N. Cong, X. Wei, X. Zhang, W. Luo, J. He, and R. Yang, "Realization of multiband communications using different Rydberg final states," *AIP Adv.*, vol. 12, no. 6, p. 065118, Jun. 2022.
- [21] A. K. Robinson, N. Prajapati, D. Senic, M. T. Simons, and C. L. Holloway, "Determining the angle-of-arrival of a radio-frequency source with a Rydberg atom-based sensor," *Appl. Phys. Lett.*, vol. 118, no. 11, p. 114001, Mar. 2021.
- [22] Y. Guo, X. Guo, Y. Wang, M. Di Renzo, and P. Zhang, "Aoa detection using a single Rydberg atomic receiver: Leveraging inner-vapor interference," *IEEE Trans. Commun.*, vol. 73, no. 12, pp. 14 828–14 844, 2025.
- [23] F. Zhang, B. Jin, Z. Lan, Z. Chang, D. Zhang, Y. Jiao, M. Shi, and J. Xiong, "Quantum wireless sensing: Principle, design and implementation," in *Proc. Annu. Int. Conf. Mobile Comput. Netw. (ACM MobiCom'23)*, Oct. 2023, pp. 1–15.
- [24] M. Chen, T. Mao, Z. Zhu, H. Feng, G. Gao, Z. Wu, W. Xiao, Z. Li, and D. Zheng, "High-resolution quantum sensing with Rydberg atomic receiver: Principles, experiments and future prospects," *arXiv preprint arXiv:2506.11833*, Jun. 2025.
- [25] D. Arumugam, J.-H. Park, B. Feyissa, J. Bush, and S. P. M. Nagaraja, "Remote sensing of soil moisture using rydberg atoms and satellite signals of opportunity," *Phys. Rev. Appl.*, vol. 21, p. 044025, Apr. 2024.
- [26] M. Chen, T. Mao, Y. Zhao, W. Xiao, D. Zheng, Z. Wang, J. Zhang, and S. Chen, "New paradigm for integrated sensing and communication with Rydberg atomic receiver," *arXiv preprint arXiv:2506.13304*, Jun. 2025.
- [27] H. Wu, X. Yao, C. Xie, K.-D. Wu, S. Wu, R. Ni, G.-Y. Xiang, and C. Gong, "On-off keying signal detection based on hidden markov model for Rydberg atomic sensor," *IEEE Trans. Commun.*, 2025.
- [28] J. Zhu and L. Dai, "General signal model and capacity limit for Rydberg quantum information system," *arXiv preprint arXiv:2506.23455*, Jun. 2025.
- [29] S. Yuan, M. Jing, H. Zhang, L. Zhang, L. Xiao, and S. Jia, "Isotropic antenna based on Rydberg atoms," *Opt. Express*, vol. 32, no. 5, pp. 8379–8388, Feb 2024.
- [30] Y. Chen, X. Guo, C. Yuen, Y. Zhao, Y. Guan, C. M. S. See, M. Debbah, and L. Hanzo, "Harnessing Rydberg atomic receivers: From quantum physics to wireless communications," *arXiv preprint arXiv:2501.11842*, Jan. 2025.
- [31] L. Sanguinetti, A. A. D'Amico, and M. Debbah, "Wavenumber-division multiplexing in line-of-sight holographic MIMO communications," *IEEE Trans. Wireless Commun.*, vol. 22, no. 4, pp. 2186–2201, Apr. 2023.
- [32] Z. Wan, J. Zhu, Z. Zhang, L. Dai, and C.-B. Chae, "Mutual information for electromagnetic information theory based on random fields," *IEEE Trans. Commun.*, vol. 71, no. 4, pp. 1982–1996, Apr. 2023.
- [33] H.-T. Tu, K.-Y. Liao, H.-L. Wang, Y.-F. Zhu, S.-Y. Qiu, H. Jiang, W. Huang, W. Bian, H. Yan, and S.-L. Zhu, "Approaching the standard quantum limit of a Rydberg-atom microwave electrometer," *Sci. Adv.*, vol. 10, no. 51, p. eads0683, 2024.
- [34] C. L. Holloway, M. T. Simons, J. A. Gordon, A. M. Dienstfrey, D. A. Anderson, and G. Raithel, "Electric field metrology for SI traceability: Systematic measurement uncertainties in electromagnetically induced transparency in atomic vapor," *J. Appl. Phys.*, vol. 121, pp. 233 106–233 106, Jun. 2017.
- [35] T. Gong, A. Chandra, C. Yuen, Y. L. Guan, R. Dumke, C. M. S. See, M. Debbah, and L. Hanzo, "Rydberg atomic quantum receivers for classical wireless communication and sensing," *IEEE Wireless Commun.*, pp. 1–11, 2025.

- [36] R. Méndez-Rial, C. Rusu, N. González-Prelcic, A. Alkhateeb, and R. W. Heath, "Hybrid MIMO architectures for millimeter wave communications: Phase shifters or switches?" *IEEE Access*, vol. 4, pp. 247–267, Jan. 2016.
- [37] Edmund Optics, "Anti-reflection (AR) coatings," 2025. [Online]. Available: <https://www.edmundoptics.com/knowledge-center/application-notes/lasers/anti-reflection-coatings>
- [38] A. Ndjiongue and H. Ferreira, "An overview of outdoor visible light communications," *Trans. Emerging Telecommun. Technol.*, vol. 29, no. 7, p. e3448, Jul. 2018.
- [39] S. Zhong, *Antenna theory and techniques*. Publishing House of Electronics Industry, 2011.